

# Systems for Breast Tumor Detection Using Microwave Imaging

Catarina Alexandra Godinho Rebocho  
*Instituto Superior Técnico*  
Lisbon, Portugal  
rebochocatarina@gmail.com

**Abstract**—Breast cancer is the most prevailing form of cancer among women. However, conventional preliminary diagnoses are harmful, painful, time consuming and money costly for mass population screening. These drawbacks motivated the research for alternatives for early detection of breast cancer. This paper proposes and demonstrates a breast cancer detection system based on microwave radiation. The paper includes two main correlated topics: de-embedding of dielectric properties of biological tissue samples, and microwave imaging. The first topic is based on the open-ended coaxial cable method. We numerically studied its sensitivity with well-known characterized samples, and experimentally measured the permittivity of animal tissues and some liquid mixtures that mimic the breast. Two of them have similar properties of tumor and fat, which constitute our breast phantoms for the second part of the work. The second topic concerns microwave imaging to extract the tumor response from the breast phantoms. To this end, a modified broadband Vivaldi antenna was designed and tested, both alone and in a circular array configuration. The experimental results corroborate the numerical results, which show an image improvement when using multiple antennas and selecting specific links between them. In order to ease the equipment handling, an user-friendly graphical interface was also developed to automate the measurement procedure. Also a switching circuit was designed and fabricated to allow multiple antenna management.

**Index Terms**—Breast cancer, complex permittivity measurement, microwave imaging, broadband antenna, switching network, measurement setup.

## I. INTRODUCTION

Breast cancer is the most prevailing type of cancer among women and the second cause of death by cancer [1]. Nowadays, the most used methods in breast cancer detection are x-ray mammography, magnetic resonance imaging and ultrasound [2]. Mammography requires breast compression, which is painful, and exposes the patient to ionizing radiation. Moreover, for dense breast tissues, the tumor may be masked due to low contrast between malignant and normal tissues, leading to false-positive test results and follow-up examinations. Magnetic Resonance Imaging (MRI) uses magnetic fields to produce high resolution images of the breast, but it is an expensive and longstanding procedure. Ultrasound uses sound waves to reconstruct the internal structure of the breast. It is a painless examination and does not expose the patient to radiation, but shows small resolution, takes a long time and its effectiveness depends on the operator responsible for the exam. The drawbacks of the aforementioned screening methods, motivated the research for complementary breast

imaging technologies, such as microwave imaging (MWI) for its non ionizing and painless nature, which poses no health risk and avoids breast compression, as well as the low costs associated. MWI relies on the contrast between healthy tissues and the tumor. The difference in permittivity causes the backscattering of microwave energy that is picked up by sensors distributed around the breast. From these echoes and using adequate signal processing algorithms, it is possible to reconstruct an image of the breast tissues. In the field of MWI, it is common to categorize active MWI as tomography and radar-based. Microwave tomography aims at reconstructing the breast profile based on dielectric properties, using non-linear inversion algorithms. Radar-based MWI concerns the detection of significant scatterers (e.g. breast tumor) overcoming the computational challenges of microwave tomography.

Regarding the dielectric properties measurements, several methods are used in order to determine the complex permittivity of a sample, such as transmission/reflection line method [3], resonant method [4], open-ended coaxial probe method [5] and free space method [6]. The transmission/reflection line method uses coaxial lines or waveguides to measure the complex permittivity of samples. This method is suitable for lossy and low loss solid SUTs, in order to fit tightly in the gap section, at the cost of being sensitive to air gaps between the sample and waveguide/coaxial line, which may induce errors in the measurements. The resonant method is one of the most accurate methods to measure permittivity of samples. However, this method is suitable for solid and non-solid samples, and only a single frequency can be measured for each sample. Free space method is non destructive, broadband and contactless. It uses two antennas facing each other and the sample holder is placed between them, but requires large and thin samples under high temperature materials and shows diffraction effects on the edges of the sample. The open-ended coaxial probe method is widely used for liquid and semi-solid samples and requires submersing the tip of the cable and measuring the reflection coefficient from which we de-embed the permittivity of SUT. It presents many advantages, such as simple construction, single measurement point, and it is broadband. The main limitation of this method is the formation of air gaps between the probe and the sample. Regarding microwave imaging, we can find in the literature different types of antennas for medical microwave imaging such as monopole-based [7], dipole-based [8], bowtie [9], though they

lack stable radiation characteristics with frequency, horn antennas [10] size limits the number of probes around the breast. Vivaldi antenna was first proposed by P. J. Gibson in 1979 [11]. Vivaldi antennas are good candidates for medical MWI due to their compact dimensions and fairly directive radiation patterns. Vivaldi is like a travelling-wave type antenna and has an exponential tapered profile, which provides large bandwidth and end-fire radiation patterns. Also, its simple construction, compact design and low costs associated makes the Vivaldi antenna suitable for microwave imaging methods. However, its significant large size is a limitation to systems which require multiple antennas. Thus, decreasing its dimensions represents a challenge, maintaining the bandwidth.

This dissertation is organized in four chapters, and each chapter is divided in two sections, regarding the two main topics to be addressed:

- Dielectric properties of samples;
- Microwave breast imaging.

Section II presents the formulation used to measure dielectric properties of tissues and microwave breast imaging. Section III addresses the numerical study of dielectric properties of samples, which include probe design and simulated results, and the study of microwave breast imaging, including the setup and switching network manufacturing. Section IV regards dielectric properties measurements and MWI experimental, with follow-up discussion. Finally, section V draws the main conclusions of the work, which includes future work description.

## II. ANALYTICAL FORMULATION

This section discusses the analytical background of the open-ended coaxial probe, which we used for dielectric measurement of biological tissues and liquids, and the formulation of the imaging algorithm for the reconstruction of the reflectivity map of breast tissues.

### A. Open-Ended Coaxial Probe Method

In order to characterize the electrical properties of the tissues, we immerse the tip of the probe in the material under test (MUT) and measure the reflection coefficient using a vector network analyzer (VNA). The electromagnetic field is extremely focused on the tip of the probe. Figure 1 shows the probe immersed into the MUT.

The input reflection coefficient measured with the MUT at the tip of the probe,  $S_{11}^{MUT}$ , is related to  $A_1$ ,  $A_2$  and  $A_3$  [12] through,

$$S_{11}^{MUT} = \frac{A_2 + A_3(\epsilon'_r - j\epsilon''_r)}{A_1 + (\epsilon'_r - j\epsilon''_r)}. \quad (1)$$

Rearranging expression 1, the complex permittivity can be de-embedded as

$$\epsilon_r = \epsilon'_r - j\epsilon''_r = \frac{S_{11}^{MUT} A_1 - A_2}{A_3 - S_{11}^{MUT}}. \quad (2)$$

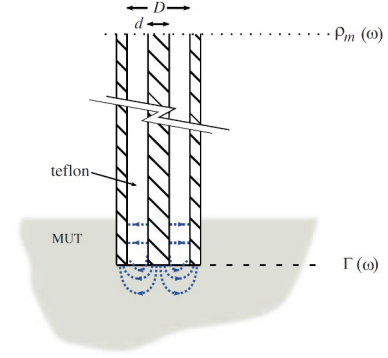


Fig. 1. Probe tip immersed in MUT [12].

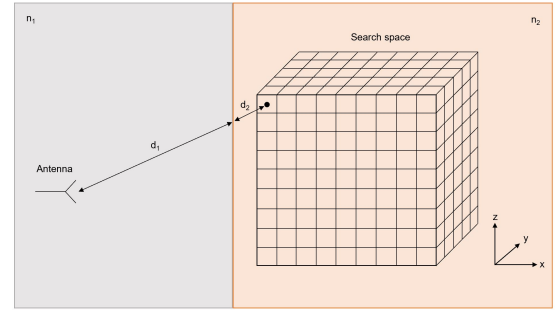


Fig. 2. Search space containing the target. Each focal point scatters the signals transmitted by the antenna, which travel at different velocities according to the refractive index of the medium.

### B. Imaging Algorithm

The imaging method is based on wave migration, which "back-propagates" the wavefront. Contrarily to radar systems, which are based on time signals, this algorithm accounts for the phase-delay of the propagating wave. It is also very time-efficient and presents the advantage of being compatible with dispersive media.

The imaging algorithm considers a search space which contains the target, as shown in Fig. 2. The location of the target is unknown.

The algorithm assumes each test point  $(x, y, z)$  as a potential scatterer. In order to obtain a detection of the target, the algorithm consists in, for every point  $p$  of the search space, multiplying the phase of the reflected wave by the frequency dependent S-parameters, for each position of the antenna  $a$ , as shown in Eq. 3.

$$v(p) = \sum_{p=1}^{t_p} \sum_{a=1}^{t_a} S(a) * e^{2jk(n_1 d_{s1}(a,p) + n_2 d_{s2}(a,p))} \quad (3)$$

where  $t_p$  and  $t_a$  are the total number of points in the search space and the total number of antenna positions, respectively.  $d_{s1}$  and  $d_{s2}$  represent the distance between the antenna and the searching scatter point.  $v(p)$  contains the final reflectivity map.

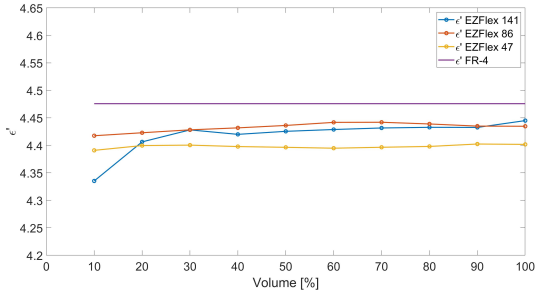


Fig. 3. Permittivity results for FR-4 versus the percentage of the original sample volume, for the three probes. Solid curve represents the expected value of FR-4 permittivity, extracted from CST material database. Curves with symbols represent the results de-embedded from CST simulation, for the three probes.

This phase cancellation represents the comparison between the target distances and the scanning distances. When both the distances become equal, the phases cancel and the electric field is maximum, resulting in target detection. If the distances are different, the phases sum, meaning that there is no detection of the target. Thus, the imaging algorithm used is extremely computationally efficient and it is robust enough to overcome errors during the measurements.

In order to guarantee that the algorithm processes uniquely the target reflections, it is necessary to subtract a calibration measurement, improving algorithm performance and, consequently, have better imaging results. This way, we eliminate setup influence, such as skin reflections that may mask the tumor, and the additional length introduced by the coaxial cables and the antenna itself. Although this technique cannot be put in practice in realistic examinations, the aim of this work is the antenna characterization and the setup for MWI, and not image inversion algorithms, which can be implemented in the future.

### III. NUMERICAL RESULTS

This section starts by describing the numerical results of permittivity estimation using the open-ended coaxial probe, followed by the numerical results for microwave breast imaging, including the description of the antenna optimization steps, and the different measurement scenarios and antenna configurations.

#### A. Coaxial Probe Design

We chose three coaxial cables, EZFlex 141, EZFlex 86 and EZFlex 47 [13], and the order of presentation is from the larger to the thinnest. The probes were calibrated in open circuit, short circuit and terminated with a Teflon sample. Afterwards, we simulated a FR-4 ( $\epsilon_r = 4.4$ ,  $\tan(\delta) = 0.018$ ) sample of volume  $4 \times 4 \times 3$  cm<sup>3</sup>. We successively reduced the original sample dimensions by 10% steps, until the smallest possible size that could provide satisfactory results of the permittivity. Fig. 3 shows the permittivity results for FR-4 versus the variation of volume size, from 10% up to 100%, at 1 GHz, for the three probes, using Eqs. 1 and 2 from Section II.

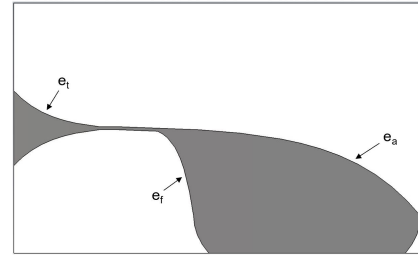


Fig. 4. BAVA design with curvature parameters.

We observe that permittivity values of FR-4 with EZFlex 141 and 86 are closer to the expected value than EZFlex 47, although the difference is about 1.5%. Moreover, for small volumes, permittivity values were expected to have the bigger discrepancy, and EZFlex 47 shows better performance measuring small samples than the other two probes, with a more consistent behaviour. We can conclude this method is really sensitive to volume sample and probe size, but it is possible to reduce the sample size and still obtain useful results. The challenge faced by EZFlex 47 is that it is very thin which compromises its mechanical rigidity. When we press the probe against the sample to submerge the tip, the probe may easily bend, and produce errors in the measurements. EZFlex 86 is the chosen probe for experimental measurements and it was fabricated.

#### B. Microwave Imaging Numerical Results

The initial Vivaldi antenna design is shown in Fig. 4, including its geometric parameters, and it is a Balanced Antipodal Vivaldi Antenna (BAVA). The substrate used is a Rogers RT5880, with thickness 0.254 mm and dielectric properties  $\epsilon_r = 2.2$  and  $\tan(\delta) = 0.0009$ . The exponential profiles of the copper layers,  $e_a$ ,  $e_f$  and  $e_t$ , are defined by the Eq. 4, and its curvature parameters are defined in [14].

$$z = \pm A_{a,f,t} * e^{P_{a,f,t}(x - B_{a,f,t})} + C_{a,f,t} \quad (4)$$

The final antenna design took several steps in order to achieve the maximum possible optimization. Given that the purpose of the antenna is to be distributed around the breast, we re-shaped the antenna substrate into a trapezoid. This polygon is compatible with the sought circular configuration. This modification allows to expand the ellipse size, which greatly influences the minimum operation frequency. The electric currents at the lower band are mostly concentrated on the top edge of the antenna, so enlarging these dimensions provides better impedance matching at these frequencies. In order to improve the directivity at lower frequencies, we added a slot at the edge of the ellipse. The slot forces the currents to circulate around it and, therefore, minimize the radiation in non-intended directions. The final antenna design was called Circular Array BAVA (CABAVA) and it is illustrated in Fig. 5. Fig. 6 shows the  $S_{11}$  of CABAVA.

Our CABAVA is still facing dimension issues, because aperture size is only 2 mm smaller than the initial design of BAVA.

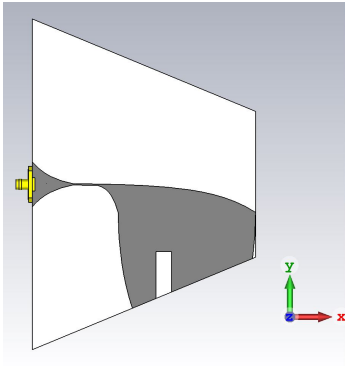


Fig. 5. CABAVA.

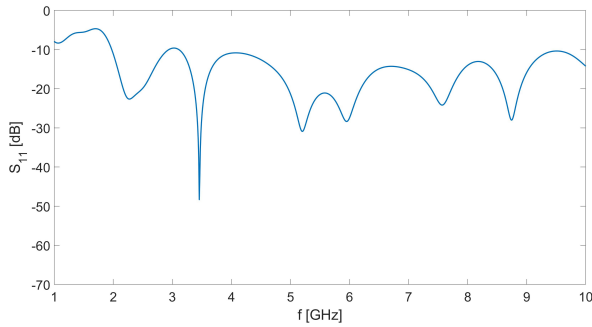


Fig. 6. BAVA  $S_{11}$  with ellipse and substrate extension, in a trapezoidal geometry, with slot inclusion.

This aperture size determines the number of elements that can be arranged in the circular configuration of antennas but also to optimize the space necessary to accommodate the antennas. Fig. 7 shows the final circular configuration with 8 CABAVA, with internal radius 60 mm, which represents a set of antennas. The isolation between the antennas is approximately 15 dB, which represents a good trade-off between antenna separation and energy coupling.

We added a dielectric cylinder that represents the breast in

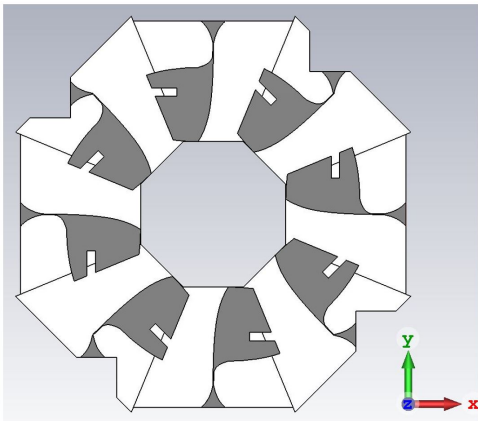


Fig. 7. Final circular configuration of 8 CABAVA, with internal radius 60 mm.

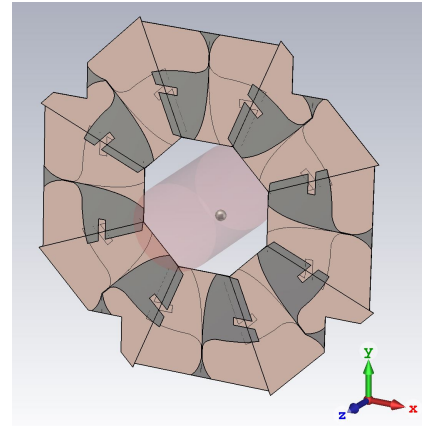


Fig. 8. Circular configuration of 8 CABAVA, with one metallic cylinder submersed in dielectric, at  $(x_s, y_s, z_s) = (15, -5, 0)$  mm.

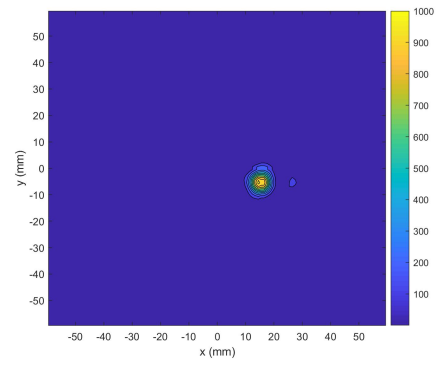


Fig. 9. Reconstructed image of XY plane at  $z = 0$  mm, with a metallic sphere embedded in the dielectric cylinder. Both monostatic and bistatic (between adjacent antennas) information were accounted.

a first approach, with  $\epsilon_r = 4$  and  $\tan(\delta) = 0.1$ . The dielectric cylinder is centered in the origin, has length of 12 cm and 8 cm diameter. A metallic sphere is submersed in the dielectric cylinder at  $(x_s, y_s, z_s) = (15, -5, 0)$  mm. Fig. 8 illustrates the description. This scenario is challenging due to the fact that we have to consider different propagation velocities according to the propagation material, assuming that we know the shape and dimension of the dielectric. Moreover, there is a large reflection of the air-body interface that hinders the detection of the target embedded in the body. In this study we eliminate it by simulating the same setup with and without target, which should only keep the target response.

Fig. 9 shows the reconstructed image after applying Eq. 3, with a 1:10 contrast between the metallic sphere and the surrounding dielectric medium. The imaging algorithm processed the monostatic information, plus bistatic information between side-by-side antennas (adjacent antennas). The metallic sphere was correctly detected.

Afterwards, we added a second set of antennas, rotated by  $22.5^\circ$ , as shown in Fig. 10. We want to know how the results differ, with the presence of multiple sets, and they are presented in Fig. 11. Comparing the intensity values with

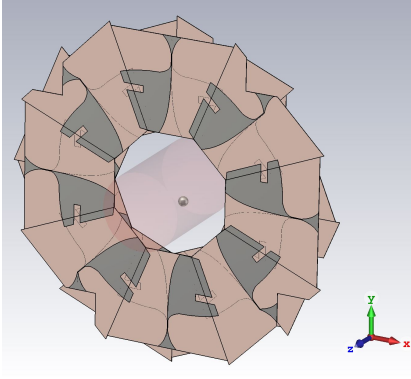


Fig. 10. Circular configuration of 16 CABAVA distributed by two levels, with one metallic sphere submersed in dielectric medium, at  $(x_s, y_s, z_s) = (15, -5, 0)$  mm.

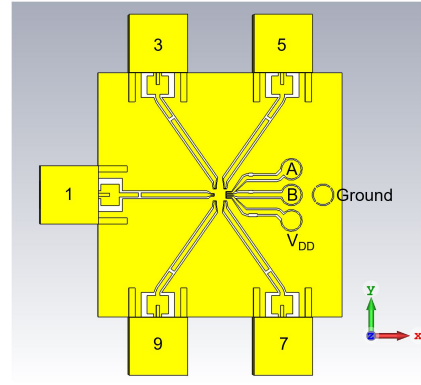


Fig. 12. SP4T switch.

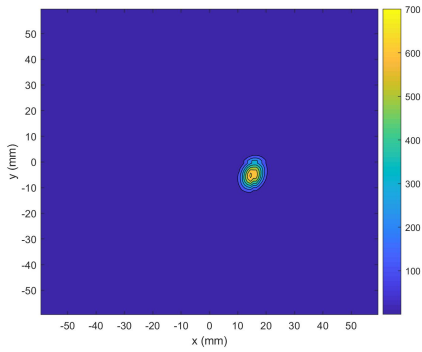


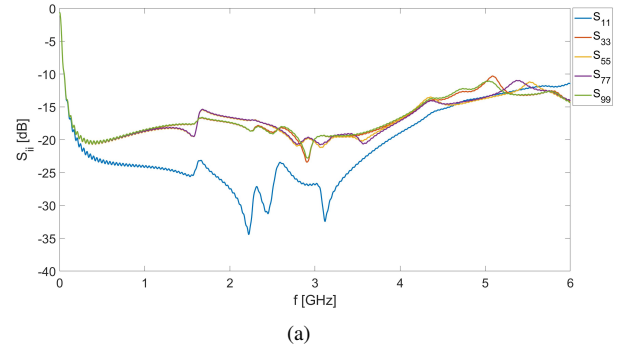
Fig. 11. Reconstructed image of XY plane at  $z = 0$  mm, with a metallic sphere embedded in the dielectric cylinder. Monostatic plus bistatic information between the antennas of different levels, plus adjacent antennas.

Fig. 9, they lowered with two sets of antennas, from 1000 to 700, although the target was clearly detected. XZ and YZ planes are not included, since the resolution along the  $z$ -axis is low, even with two sets of antennas. Thus, we conclude that there is no advantage in using two sets of antennas due to the significant mutual coupling between them, which degrades the image quality.

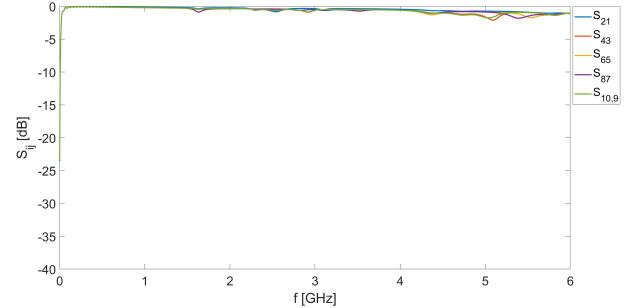
### C. PCB design

In an attempt to use more than four CABAVA with a 4-port VNA, a SP4T switch [15] is required to commute between the antennas. We need to insert the switch in a PCB circuit, in order to properly connect the switch pins to SubMiniature version A (SMA) connectors and direct current (DC) poles. The design of the PCB was based on this datasheet [15] and build in CST Studio Suite, to operate in the frequency band 0.1 GHz - 6 GHz. The circuit has two copper layers and the substrate used is FR-4, and it is illustrated in Fig. 12.

A VNA is connected to port 1 of the PCB as the source signal. Ports 3, 5, 7 and 9 are the outputs to connect the antennas. The signal inputted to port 1 is conducted to one of the four output ports, accordingly to the antenna we want to select. Only one path is opened at a time and its selection



(a)



(b)

Fig. 13. Simulated S-parameters from the switch. (a) Reflection coefficients  $S_{11}, S_{33}, S_{55}, S_{77}, S_{99}$ . (b) Transmission coefficients  $S_{21}, S_{43}, S_{65}, S_{87}, S_{10,9}$ .

is performed by inputting a sequence of two binary digits, represented by A and B, as we can see in Fig. 12.

At this point, to analyze the performance of the switch, we only need to account for the results of the scattering parameters, as they were simulated and presented in Fig. 13. We want to have maximum transmission along the coplanar lines and minimum reflection ( $|S_{11}| \leq -15$  dB and  $|S_{21}| \approx 0$  dB), which is corroborated in Fig. 13. Since the switch revealed positive results, we conclude it is functional and it was fabricated.

#### IV. EXPERIMENTAL RESULTS

This section addresses the experimental results of permittivity measurements and microwave breast imaging, as it is divided in two sub-sections. The first sub-section presents the open-ended coaxial probe method experimental results for de-embedding the relative permittivity of liquid and semi-solid samples. The second sub-section regards the measurement setup used for microwave breast imaging, including the breast phantom and the distribution of the antennas around the breast, followed by the description of the developed user-friendly graphical user interface that helps technicians and doctors performing the examination. Afterwards, the results of microwave breast imaging are presented, with two different antennas, as well as the results of the new designed switching network.

##### A. Permittivity Measurements Experimental Results

The purpose of these measurements is to study the sensitivity of open-ended coaxial cable method to the probe contact with materials of different hardness and heterogeneity, different water content, and sample size.

The probe EZFlex 86 was calibrated in open circuit, short circuit and terminated with distilled water. We selected distilled water (instead of Teflon as in the numerical analysis of Section III) because this method is not suitable for solid samples, and also distilled water is a well documented reference liquid.

Our research team already previously measured permittivity results for tumor and fat liquid mixtures. Thus, Fig. 14 shows the comparison between those results and the ones measured during this work. Fat has a lot of distortion in the measured permittivity, and at 1 GHz it is about 20% above the expected permittivity, while tumor has a deviation of less than 1%. This difference becomes smaller as frequency increases, therefore the results are considered acceptable. The method used in [16] also has a substantial uncertainty, thus we cannot conclude which one is more correct. Moreover, when changing between liquids, we cleaned the probe with ethanol. We found out later that the alcohol impregnated the teflon of the probe, which contributed to increase the error of the measurements.

We also measured solid samples, but the inevitable air gaps, and possible probe bending distorted the results.

Lastly, we tested the probe in animal tissues: beef and pork belly. Beef is mostly muscle and pork belly is fat. Thus, muscle permittivity ( $\epsilon_r \simeq 50$ ) is higher than fat permittivity ( $\epsilon_r \simeq 5$ ), due to higher content of water [17]. In order to avoid air gaps between the probe and the sample, we applied as much pressure on the tissue as possible without bending the probe.

We started with the original beef (large) sample, with  $80 \times 42 \times 24 \text{ mm}^3$ , and have successively cut the sample in half, until the smallest acceptable sample we could be measured, which has had dimensions  $4 \times 4 \times 2 \text{ mm}^3$ . Fig. 15 shows permittivity values for the number of samples, from higher volume to lower sample volume, at 1 GHz. The point of sample to be measured was always the same, and preferably an area with low content of fat. In the first half of measurements, the

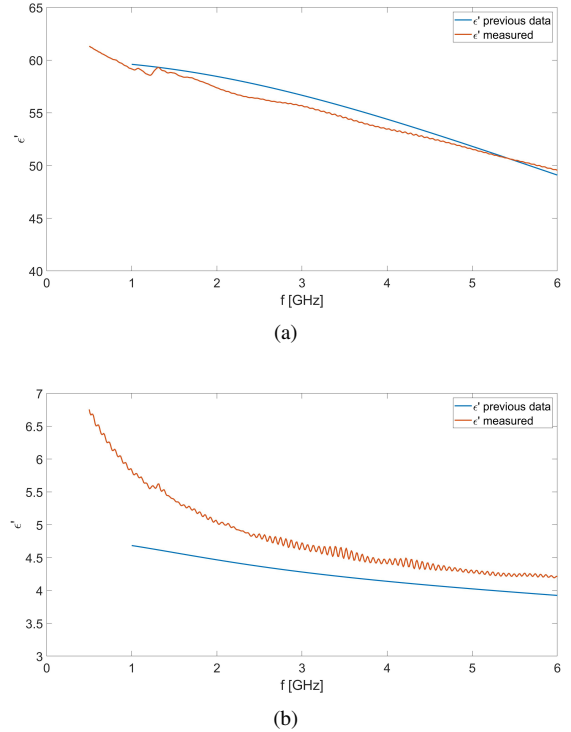


Fig. 14. Permittivity of liquid samples along the frequency range. Blue curve represents previous data from our research team and red curve the measured permittivity during this work. (a) Tumor mixture. (b) Fat mixture.

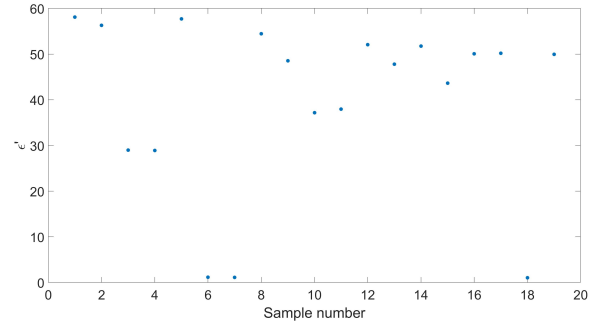


Fig. 15. Permittivity results for the number of beef samples, from higher to lower volume, at 1 GHz, considering always the same sampling point.

results show higher variation than the second half. This may be due to incorrect pressure over the sample. First we reduced the sample by almost half the larger dimension, and then the reductions become smaller. Thus, we may infer that the sample volume no longer influenced the last seven measurements. Sample volumes number 6, 7 and 18 did not show useful results probably due to incorrect pressure of the probe. This pressure also shows some limitations, not just probe bending, but also water accumulation around the probe tip, which may produce false results. Overall, the heterogeneity nature of beef sample, over the sample volume, is a clear limitation to this method.

Afterwards, the fat sample was reduced twelve times, from

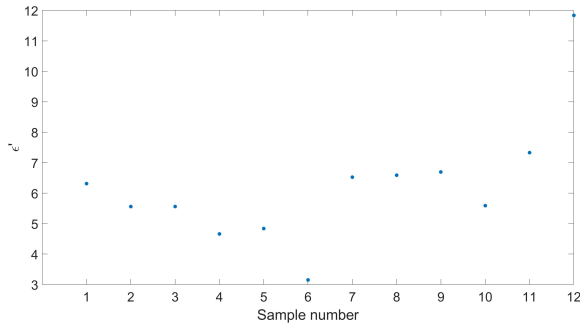


Fig. 16. Permittivity results for the number of fat samples, from higher to lower volume, at 1 GHz, considering always the same sampling point.

the original sample with  $75 \times 30 \times 27 \text{ mm}^3$ , until the sample failed to allow reliable measurement of the permittivity, which has dimensions  $6 \times 4 \times 5 \text{ mm}^3$ . We measured the same point in the sample, during the twelve measurements. Fig. 16 shows permittivity results of the fat sample, for the number of samples, from higher volume to lower sample volume, at 1 GHz. Sample volumes 6 and 12 may have had errors during the measurement due to incorrect pressure over the sample.

The results are acceptable and we can conclude that the coaxial cable method to determine complex permittivity of tissue samples is really sensitive to the pressure applied to the sample. Tissue heterogeneity also influences the results but it is a limitation inherent to the sample. However, the method is not sensitive to sample size variations, since the results are reasonably consistent along the variation of the volume sample, excluding the ones due to inconsistent pressure. Besides, it is important to clean the probe with alcohol free products or even non-liquid products, because it may impregnate the probe by capillarity and degrade the results.

### B. Experimental Results of Microwave Breast Imaging

Regarding the measurement setup, the real application will consist in a bed, where the patient lies on prone posture, with a circular opening where the breast is pending. The best approach in the lab was based on a plexyglass platform in order to be transparent, allowing to see the setup. The breast is represented by an MRI-derived phantom [18] that was 3D-printed using PLA. The breast container was filled with a homogeneous mixture which mimics the dielectric properties of fatty tissues. This mixture was already characterized in the previous section III. The probe antennas are distributed around the phantom. As in a real exam, the antennas are allowed to move vertically, in order to ensure adequate resolution along the vertical axis. The measurement setup is shown in Fig. 17.

Moreover, we developed a graphical interface which is intended to be used by technicians and doctors. This interface allows a simple interaction of the user with the instruments and devices, requiring from them little knowledge on how to control them. It automates the measurement process, thus facilitating the usage of this technology. The purpose of the application is to emulate the instrument environment

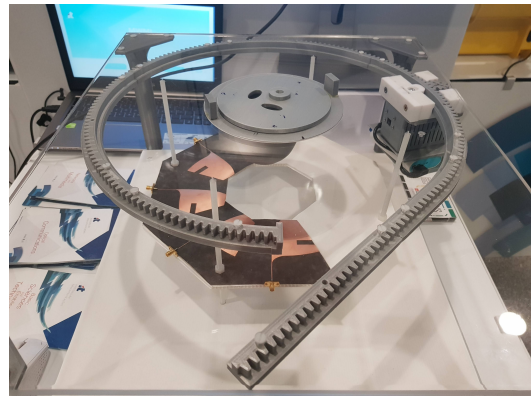


Fig. 17. Measurement setup.

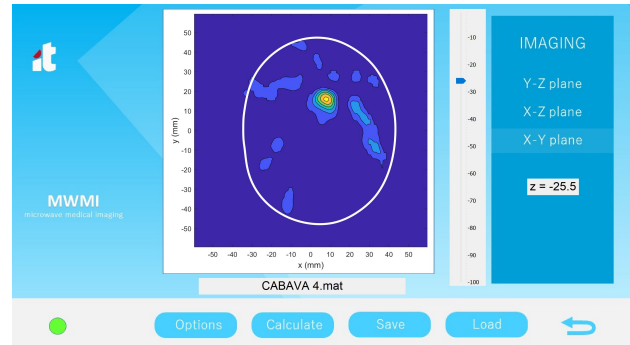


Fig. 18. Example of a reconstructed image resulting from a lab measurement, using the graphical interface. 2D slice of XY plane at  $z = -25.5 \text{ mm}$ .

that can be used for a complete clinical exam. The graphical interface is divided in three parts. The first part regards to the Setup menu that allows the equipment technicians to prepare the setup for the exam. The second menu, Calibration, is also intended to be used by technicians. It concerns the calibration of the antenna rewiring network through the switch. This functionality was not implemented, thus it does not have sub-menus associated. The third menu, Imaging, is intended for the medical staff performing the examination. The medical doctor may observe the three main planes: XY, YZ and XZ planes, in search of a possible tumor inside the patient's breast, as illustrated by Fig. 18. In order to help in the perception of the breast size and tumor location, it is also presented the breast contour in the reconstructed images. Fig. 18 shows an example of an image reconstructed from a lab measurement, with a single CABAVA on breast phantom. The white line represents the breast contour and target center location is at  $(x, y, z) = (10, 20, -26) \text{ mm}$ . The calculations take about 9 minutes, in a computer with an Intel Core i7 processor, occupying 1 GB RAM; note that the examination duration may be shortened by adjusting the desired resolution of the final image (at the cost of less detail), which can be also done in the interface.

Next, the experimental results of microwave imaging using the measurement setup previously described are presented. The



Fig. 19. 1-element CABAVA.

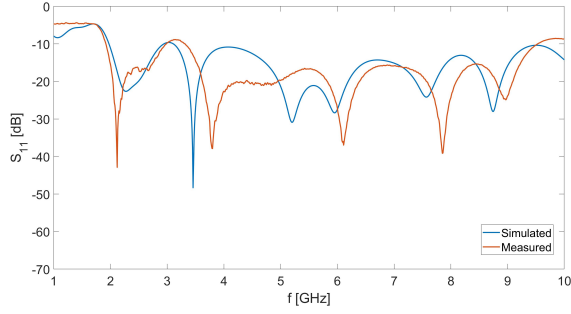


Fig. 20. Comparison between simulated and measured  $S_{11}$  of CABAVA.

CABAVA antenna was fabricated and it is shown in figure 19.

The  $S_{11}$  was measured with the CABAVA in free space, along the frequency range of 1 GHz - 10 GHz. The simulated  $S_{11}$  from Fig. 6 is shown in Fig. 20 for easier comparison with the  $S_{11}$  measured in lab. The results show good agreement all over the frequency range. The small discrepancies are attributed to manufacturing imprecision and numerical inaccuracies.

We image the breast using a single antenna element for one position of the tumor, at a single height of  $z = -18$  mm. The measurement frequency range is 2 GHz - 7 GHz. The results are shown in Figs. 21 for one position of the tumor. 1 mm resolution was used to reconstruct the images, and the power of the electric field absolute value is represented. Only monostatic information was accounted in the imaging algorithm. Also, low resolution was obtained along the  $z$ -axis, thus XZ and YZ planes are omitted.

Although there are some artifacts which are due to small misalignment between the antenna and the breast, the tumor was successfully detected and it is easily identified. Afterwards, the 4-element CABAVA was fabricated and it is shown in Fig. 22.

Additionally, we took more measurement points, by moving the 4-port CABAVA vertically. The measured  $z$ -coordinates were:  $z = -32$  mm,  $z = -42$  mm and  $z = -51$  mm. We merged the information from the three coordinates to simulate three antenna sets and the results are shown in Fig. 23.

We concluded that there is a clear improvement on the re-

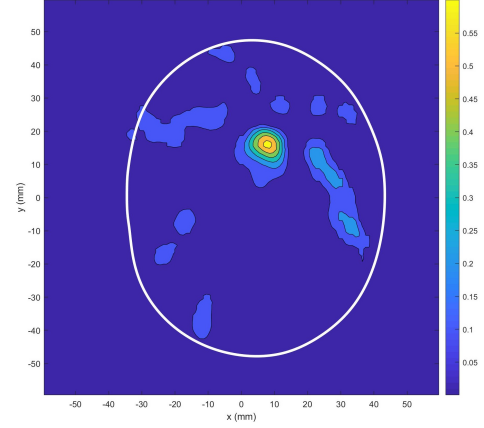


Fig. 21. 2D images of slice through the inclusion at  $(x, y, z) = (10, 15, -25)$  mm. The white lines define the breast phantom contour.



Fig. 22. 4-element CABAVA.

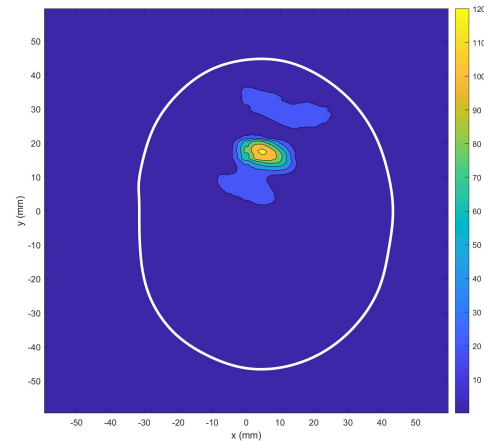


Fig. 23. 2D reconstructed images of slices through the tumor in first position at  $(x, y, z) = (10, 15, -35)$  mm. Merged results of antenna coordinates at  $z = -32$  mm,  $z = -42$  mm and  $z = -51$  mm. XY plane at  $z = -35$  mm.

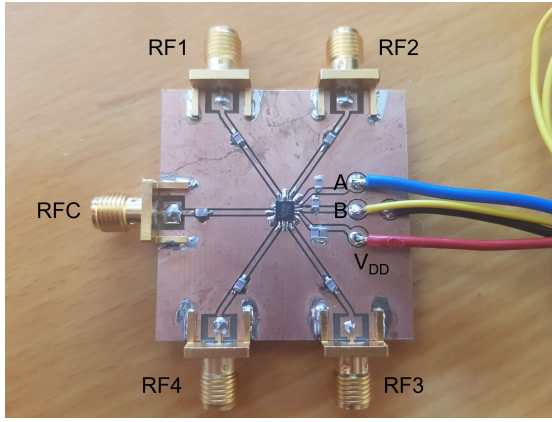


Fig. 24. Fabricated PCB with the SP4T switch.

sults from the 1-element CABAVA to the 4-element CABAVA. The increased number of antennas and the correct information chosen for data processing, give us a correct and clear detection of the target. Also, the range of intensity values increased from 1 to 120, when we scan multiple z-planes, using the 4-port CABAVA. This approach presents better results than using two sets simultaneously, represented in section III, which show a decreasing in the spectrum of intensity values. This is due to mutual coupling between the two sets, which does not constitute a problem when using one set scanning multiple z-planes.

### C. Fabricated PCB

The PCB for SP4T switch designed in section III was fabricated and it is shown in Fig. 24.

The four cables (blue, yellow, red and black) shown in Fig. 24 are connected to a Raspberry Pi. The red cable feeds the switch with 5 V and the black cable is connected to the ground. Each RF path is selected via two bits applied to the A and B control inputs, through the blue and yellow cables, respectively. We selected the RF1 path corresponding to port 2. Fig. 25 shows the measured reflection coefficients of the four ports. We want maximum transmission between RFC and RF1 (i.e. ports 1 and 2, respectively), and  $S_{11}$  and  $S_{22}$  curves should present a low magnitude level ( $\leq -15$  dB). We observe in Fig. 26 that  $S_{12}$  presents an isolation of 15 dB between port 1 and 2, when it should behave as  $S_{11}$  and  $S_{22}$  in Fig. 25. The remaining  $S_{ij}$  show an isolation below -30 dB, which is acceptable.

The results for the RF2, RF3 and RF4 paths are similar to RF1, thus they are omitted. Due to the incorrect behaviour of the S-parameters, the PCB was analyzed, with the help of the technical team. We concluded the terminations of the RF paths presented a very thin gap, in the exact location of the connection with the switch. This could be causing the most of the energy, which flows through the RF paths, to be dispersed in the metallization, instead of being transferred to the switch. This way, the PCB needs to be redesigned with larger gaps in the terminations of the RF gaps, so that it could be tested

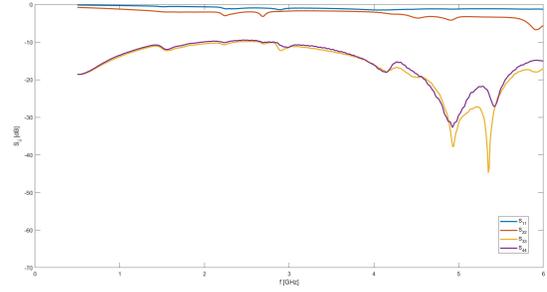


Fig. 25. Reflection coefficients when RF1 is selected.

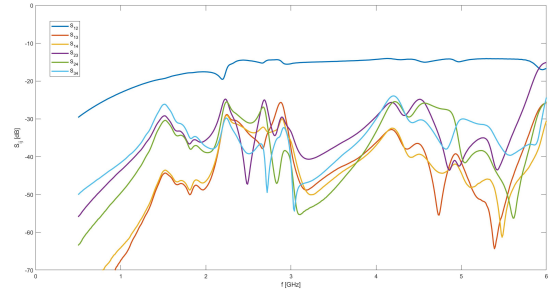


Fig. 26. Transmission coefficients when RF1 is selected.

once more and to provide the ability to use eight antennas simultaneously for the MWI experimental measurements.

## V. CONCLUSIONS

Section II addresses the study of the open-ended coaxial cable method. The method produced good results and it is suitable for liquid and semi-solid samples, but not for solid samples, due to inevitable air gaps formed between the probe tip and the SUT. The main limitation of the open-ended coaxial cable method is the high sensitivity to the pressure applied to the probe over the sample. Afterwards, a new compact antipodal Vivaldi antenna is presented and submitted to a shape evolution process, in order to achieve the best possible compromise between size and bandwidth. The final antenna was called CABAVA. Next, we simulated the set of antennas in two different scenarios: a sphere target suspended in air, and a sphere target immersed in a dielectric medium. The target was successfully detected for both cases. Afterwards, we added a second circular array, at 1 cm off z-distance, to reconstruct the images using more information. We concluded that expanding the useful information to the entire S-matrix in the imaging algorithm contributes to deteriorate the results instead of improving them and we achieved the best results for one set.

A PCB for SP4T switch encapsulation was designed in order to commute between the antenna pairs. The simulation exhibited good results, contrarily to the experimental results after fabrication. the PCB for the switching network needs to

be re-designed in order to obtain results that makes sense, as the simulated ones in CST.

Since the numerical analysis produced good results, the measurement setup was prepared in order to extract the tumor response from the breast phantom. The developed GUI executes essential steps which automate the measurement procedure. The CABAVA was fabricated and used in the experimental measurements, as well as a 4-port CABAVA. The 4-port CABAVA takes less time to perform the measurements, and the results show improvements given the 1-port CABAVA. Moreover, we scanned several z-planes with the 4-port CABAVA and when we merged that information, we observed that the results slightly improved compared to one CABAVA. This way, we concluded that the approach with one set produces better results than multiple sets used simultaneously. We did not fabricate an 8-port CABAVA due to current antenna size limitation of the fabrication process available in the lab. The entire "ring" has substantial dimensions.

#### ACKNOWLEDGMENT

This work was hosted by Instituto de Telecomunicações that provided the conditions to develop this paper, including the computational and laboratory resources. I would like to express my gratitude to Professor Carlos Fernandes and João Felício, for all the guidance, invaluable support and motivation, throughout this work.

#### REFERENCES

- [1] Cancer stat facts: Female breast cancer. <https://seer.cancer.gov/statfacts/html/breast.html>, 2018.
- [2] Christiane K. Kuhl, Simone Schradling, Claudia C Leutner, Nuschin Morakkabati-Spitz, Eva Wardelmann, Rolf Fimmers, Walther Christian Kuhn, and Hans Heinz Schild. Mammography, breast ultrasound, and magnetic resonance imaging for surveillance of women at high familial risk for breast cancer. *Journal of clinical oncology: official journal of the American Society of Clinical Oncology*, 23 33:8469–76, 2005.
- [3] J. Baker-Jarvis, E. J. Vanzura, and W. A. Kissick. Improved technique for determining complex permittivity with the transmission/reflection method. *IEEE Transactions on Microwave Theory and Techniques*, 38(8):1096–1103, Aug 1990.
- [4] Jyh Sheen. Study of microwave dielectric properties measurements by various resonance techniques. *Measurement*, 37(2):123 – 130, 2005.
- [5] T. W. Athey, M. A. Stuchly, and S. S. Stuchly. Measurement of radio frequency permittivity of biological tissues with an open-ended coaxial line: Part i. *IEEE Transactions on Microwave Theory and Techniques*, 30(1):82–86, Jan 1982.
- [6] D. K. Ghodgaonkar, V. V. Varadan, and V. K. Varadan. Free-space measurement of complex permittivity and complex permeability of magnetic materials at microwave frequencies. *IEEE Transactions on Instrumentation and Measurement*, 39(2):387–394, April 1990.
- [7] D. Gibbins, M. Klemm, I. J. Craddock, J. A. Leendertz, A. Preece, and R. Benjamin. A comparison of a wide-slot and a stacked patch antenna for the purpose of breast cancer detection. *IEEE Transactions on Antennas and Propagation*, 58(3):665–674, March 2010.
- [8] E. C. Fear and M. A. Stuchly. Microwave detection of breast cancer. *IEEE Transactions on Microwave Theory and Techniques*, 48(11):1854–1863, Nov 2000.
- [9] S. C. Hagness, A. Taflove, and J. E. Bridges. Three-dimensional FDTD analysis of a pulsed microwave confocal system for breast cancer detection: design of an antenna-array element. *IEEE Transactions on Antennas and Propagation*, 47(5):783–791, May 1999.
- [10] Xu Li, S. C. Hagness, M. K. Choi, and D. W. van der Weide. Numerical and experimental investigation of an ultrawideband ridged pyramidal horn antenna with curved launching plane for pulse radiation. *IEEE Antennas and Wireless Propagation Letters*, 2:259–262, 2003.
- [11] P. J. Gibson. The vivaldi aerial. In *1979 9th European Microwave Conference*, pages 101–105, Sept 1979.
- [12] Jake Bobowski and Thomas Johnson. Permittivity measurements of biological samples by an open-ended coaxial line. 40, 01 2012.
- [13] EZ Form Cable Corporation. *EZForm Cables Catalog*, 2018.
- [14] J. Bourqui, M. Okoniewski, and E. C. Fear. Balanced antipodal vivaldi antenna with dielectric director for near-field microwave imaging. *IEEE Transactions on Antennas and Propagation*, 58(7):2318–2326, July 2010.
- [15] Analog Devices. Nonreflective, silicon sp4t switch, 0.1 ghz to 6.0 ghz. HMC7992 datasheet, 2016.
- [16] A. Kiourti, J. R. Costa, C. A. Fernandes, A. G. Santiago, and K. S. Nikita. Miniature implantable antennas for biomedical telemetry: From simulation to realization. *IEEE Transactions on Biomedical Engineering*, 59(11):3140–3147, Nov 2012.
- [17] C Gabriel, S Gabriel, and E Corthout. The dielectric properties of biological tissues: I. literature survey. *Physics in Medicine & Biology*, 41(11):2231, 1996.
- [18] M. J. Burfeindt, T. J. Colgan, R. O. Mays, J. D. Shea, N. Behdad, B. D. Van Veen, and S. C. Hagness. Mri-derived 3-d-printed breast phantom for microwave breast imaging validation. *IEEE Antennas and Wireless Propagation Letters*, 11:1610–1613, 2012.